

Fine-Grained 3D Facial Reconstruction for Micro-Expressions

Che Sun, Xinjie Zhang, RuiGao, Xu Chen, Yuwei Wu, Yunde Jia

Abstract—Recent advances in 3D facial expression reconstruction have demonstrated remarkable performance in capturing macro-expressions, yet very few studies have focused on reconstructing micro-expressions. This novel task is particularly challenging due to the subtle, transient, and low-intensity nature of micro-expressions, which complicates the extraction of stable and discriminative features essential for accurate reconstruction. In this paper, we propose a fine-grained micro-expression reconstruction method that integrates global dynamic features capturing stable facial motion patterns with locally-enriched features incorporating multiple informative cues from 2D motion, facial priors, and 3D facial geometry. Specifically, we devise a dynamic-encoded module to extract micro-expression features for global facial motion, allowing it to leverage prior knowledge from abundant macro-expression data to mitigate the scarcity of micro-expression data. Subsequently, a dynamic-guided mesh deformation module is introduced for extracting aggregated local features from dense optical flow, sparse landmarks, and facial geometry, which adaptively refines fine-grained facial micro-expressions without compromising global 3D geometry. Extensive experiments on micro-expression datasets demonstrate the effectiveness of our method.

I. INTRODUCTION

Realistic 3D facial expression reconstruction is critical for advancing artificial intelligence systems that rely on perceptual and emotional understanding [1], [2], particularly in social robots designed for companionship and caregiving [3], [4]. Significant progress has been achieved in reconstructing macro-expressions [5], [6], i.e., long-duration and easily recognizable expressions that convey clear emotions, while few studies have focused on micro-expression reconstruction. Micro-expressions are involuntary, fleeting, and subtle (typically under 0.5 seconds) facial expressions that reveal hidden or suppressed emotions [7]. Their subtle and rapid dynamics make them particularly informative for understanding undercurrent emotion states, while also posing significant challenges for capturing and reconstructing them. In this work, we focus on faithfully reconstructing the fine-grained dynamics of micro-expressions, enhancing the ability of intelligent robots to interpret and simulate subtle human emotions.

Reconstructing 3D facial micro-expressions is non-trivial, because extracting stable and discriminative features is complicated stemming from the unique characteristics of the extremely subtle and low-intensity facial dynamics. The low-intensity signals could be easily dominated by ubiquitous noise, such as illumination changes, head movements, and sensor artifacts, hindering these delicate signals from being encoded into the feature representations. Besides, different micro-expressions often manifest as minute variations within highly overlapping facial regions due to their locally confined nature. This leads to low separability in the feature space, making it difficult to learn discriminative features that can

reliably discriminate between subtle yet semantically different affective states.

To address the issue, we propose a fine-grained micro-expression reconstruction method that integrates global dynamic features with locally-enriched features of micro-expressions. Our method encodes global dynamic features to capture holistic facial motion patterns, which provides stable spatial-temporal contextual priors to mitigate the influence of noise and enhance overall temporal consistency. We further aggregate multiple cues, including 2D motion patterns, facial semantic priors, and 3D facial geometry, thus obtaining discriminative local features through cross-modal complementarity. The integration of globally stabilized dynamics with these locally-enriched features collectively facilitates the precise reconstruction of subtle and localized micro-expressions. Specifically, we devise a plug-and-play dynamic-encoded module to extract global facial features from both RGB and optical-flow sequences, effectively leveraging prior knowledge from abundant macro-expression data to alleviate the data scarcity of micro-expressions. A dynamic-guided mesh deformation module, which fuses locally-enriched features from dense optical flow, sparse landmarks, and 3D geometry, is introduced to adaptively refine local facial details while preserving the global facial structure.

Prior to this work, there were few dedicated benchmarks for 3D micro-expression reconstruction. Therefore, we repurpose three high-frame-rate micro-expression recognition datasets of CASME [8], CASME II [9], and SAMM [10] for evaluation, because they have proven ability to capture subtle and rapid facial dynamics. Experimental results on the three datasets show the effectiveness of our method.

The main contributions of this work are summarized as follows:

- To our best knowledge, we are the first to reconstruct fine-grained 3D facial micro-expressions. Our method encodes global facial dynamics, and subsequently applies localized and detail-preserving refinements for 3D micro-expressions, constituting a coarse-to-fine framework for effective 3D facial reconstruction.
- We propose a robust feature extraction strategy that integrates global dynamics with locally-enriched multi-modal cues, effectively suppressing noise and enhancing discriminability for subtle micro-expression dynamics.

II. RELATED WORK

We review the previous works that are closely related to our method in the field of monocular 3D facial reconstruction and head avatar creation from videos.

A. Monocular 3D Facial Reconstruction

Monocular 3D facial reconstruction has seen significant advances in recent years, and existing reconstruction methods are broadly categorized into model-free [11]–[13] and model-based paradigms [5], [14], [15]. Model-free methods typically regress 3D geometry in the form of 3D meshes [12], [16], voxels [17], or implicit representations such as Signed Distance Functions [18], [19]. While these methods exhibit flexibility, they generally rely on large-scale 3D training data, which is synthetically generated using parametric face models. This dependency, however, could influence their reconstruction fidelity, as the quality and diversity of the training data are bounded by the expressiveness of the underlying generative model [5], [11], [20]. Differently, model-based methods fit the low-dimensional parameters of a statistical face model, such as the Basel Face Model (BFM) [21] or FLAME [5], [22]. To circumvent the scarcity of large-scale 3D training data, recent model-based methods have increasingly shifted towards self-supervised learning frameworks [5], [14], [22], [23]. These methods typically employ supervision from landmark re-projection and photometric consistency losses. Recent occlusion-inpainting methods like OFER [24] and EIFER [25] focus on recovering local dynamics under partial observations by using FLAME models.

While existing methods have shown impressive capability in reconstructing macro-expressions, they pay little attention to micro-expressions. Differently, our method focuses on the reconstruction of micro-expressions by integrating global dynamics and locally-enriched features to better capture their fine-grained and transient facial dynamics.

B. Head Avatar Creation

Different from monocular 3D facial reconstruction, the creation of high-fidelity animatable head avatars rely on multi-view video inputs to achieve higher robustness and visual quality [26], [27]. Most existing methods often adopt a single representation, such as meshes [28], [29], point clouds [30], [31], or implicit radiance fields [32]–[35], to model the entire head. For example, GaussianAvatars [6] uses rigged 3D Gaussians driven by a FLAME mesh, allowing high-frequency hair modeling and real-time rendering. Concurrently, GAF [36] explores monocular video input for Gaussian-based avatar reconstruction, yet remains constrained by dynamic motion blur and limited-resolution texture details compared to multi-view approaches. Recent works, such as DELTA [37] and MeGA [38], find that 3D Gaussians excel at modeling volumetric structures but struggle with fine-grained facial details, and NeRF or mesh-based methods often fail to unify high-fidelity skin and complex hair. Therefore, they turn to hybrid or component-aware representations to address these limitations.

Existing head avatar creation methods are generally designed for macro-expressions with large head movements, typically relying on multi-view inputs or substantial pose variations. Differently, our work emphasizes the reconstruction of fine-grained micro-expressions from monocular high-frame-rate videos by integrating multi-source cues.

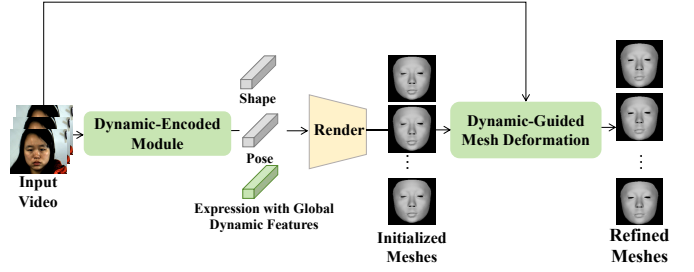


Fig. 1. The overall framework of our method.

III. PRELIMINARIES

A. Problem Formulation

Given a monocular video $V = \{I_t \in \mathbb{R}^{H \times W \times 3}\}_{t=1}^T$ with T RGB frames I_t , the goal of facial reconstruction is to estimate a detailed 3D facial geometry that faithfully captures both identity characteristics and expressive deformations. The output comprises a sequence of 3D meshes $\{\mathcal{M}_t = (\mathcal{V}_t, \mathcal{F}_t)\}_{t=1}^T$ with vertices $\mathcal{V}_t \in \mathbb{R}^{n_v \times 3}$ and faces \mathcal{F}_t in the t -th frame.

B. Analysis-by-Synthesis Paradigm

Modern learning-based approaches [5], [24] employ an analysis-by-synthesis paradigm, which consists of a face parameter encoder, a 3D face model, and a neural render for reconstructing expressive 3D faces in a self-supervised training manner.

Encoder: A deep network E^{reg} regresses the parameters of a 3D Morphable Model (3DMM) FLAME [39], given by

$$\beta_t, \psi_t, \theta_t = E^{\text{reg}}(I_t), \quad (1)$$

where β_t denotes the shape parameters, ψ_t indicates the expression parameters, and θ_t indicates the pose parameters.

3D Face Model: The FLAME model generates the 3D meshes through

$$\mathcal{V}_t, \mathcal{M}_t = \text{FLAME}(\beta_t, \psi_t, \theta_t), \quad (2)$$

which captures facial shape variations across shapes and expressions through linear blendshapes.

Neural Render: A neural image-to-image translator \mathcal{T} is introduced to achieve effective analysis-by-neural-synthesis supervision. Given a monochrome rendering of the reconstructed face mesh $S_t = R(\beta_t, \psi_t, \theta_t)$ and a sparsely input image $M(I_t)$ where only 1% of facial pixels are retained, the neural render reconstructs the original image as

$$\hat{I}_t = \mathcal{T}(S_t \oplus M(I_t)), \quad (3)$$

where \oplus denotes concatenation. This formulation forces \mathcal{T} to rely on geometric cues from S_t .

Augmented Expression Cycle Path: Starting from predicted parameters $(\beta_t, \psi_t, \theta_t)$, the expression ψ_t is replaced with an augmented version ψ_t^{aug} , and the corresponding image is generated via neural rendering $\hat{I}_t^{\text{aug}} = \mathcal{T}(R(\theta_t, \beta_t, \psi_t^{\text{aug}}) \oplus M(I_t))$. The encoder E^{reg} must recover the modified expression from the generated image, enforced by the cycle consistency between $E^{\text{reg}}(\hat{I}_t^{\text{aug}})$ and ψ_t^{aug} .

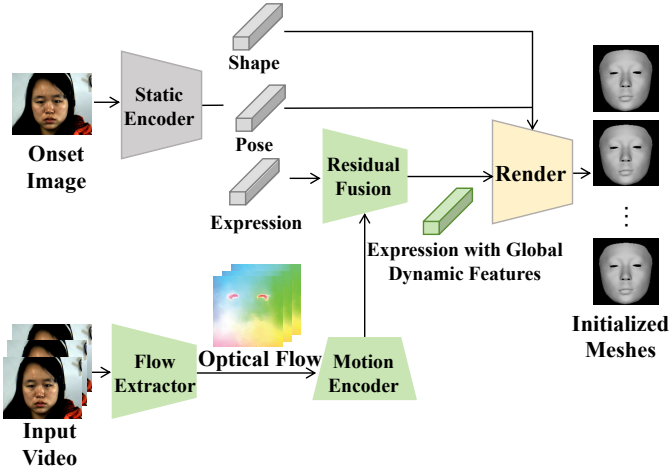


Fig. 2. The *dynamic-encoded* module generates initialized 3D facial meshes from an onset image and input video.

The analysis-by-synthesis paradigm is effective for macro-expression reconstruction, yet struggles to capture the subtle dynamics of micro-expressions. Due to their low-intensity nature, micro-expressions induce minimal dynamics in expression parameters ψ_t and facial mesh geometry \mathcal{M}_t , making it challenging to extract stable and discriminative features from such fine-grained facial dynamics.

IV. METHOD

Our method aims to reconstruct fine-grained 3D facial micro-expressions $\{\mathcal{M}_t = (\mathcal{V}_t, \mathcal{F}_t)\}_{t=1}^T$ from a monocular video V through a coarse-to-fine framework. The overall framework is depicted in Figure 1. The *Dynamic-Encoded* module takes the input video and generates initialized 3D meshes by integrating global dynamic features. The *Dynamic-Guided Mesh Deformation* module refines the initialized meshes using locally-enriched features to capture subtle dynamic details of micro-expressions.

A. Dynamic-Encoded Module

The dynamic-encoded module, illustrated in Figure 2, is designed as a plug-and-play component that generates initialized 3D facial meshes $\{\mathcal{M}_t^{\text{init}} = (\mathcal{V}_t^{\text{init}}, \mathcal{F}_t^{\text{init}})\}_{t=1}^T$ by leveraging both static shape and expression motion to extract global dynamic features.

The module operates through two parallel streams. (1) The static encoder extracts static shape β_1 , expression ψ_1 and pose θ_1 parameters from the onset image I^{onset} (i.e., I_1) serving as the anchor frame for expression dynamics. We follow the previous reconstruction work of Retsinas et al. [5] to construct the encoder by using Eq. (1), where the encoder pre-trained on abundant macro-expression data captures prior knowledge of facial expressions. (2) The flow extractor computes the optical flow sequence $\{\mathcal{O}_t \in \mathbb{R}^{H \times W \times 2}\}_{t=1}^{T-1}$ between adjacent frames I_t and I_{t+1} , and the motion encoder E^{motion} captures the subtle temporal dynamic $\Delta\psi_t$ of micro-expressions, given by

$$\Delta\psi_t = E^{\text{motion}}(\{\mathcal{O}_t\}_{t=1}^{T-1}). \quad (4)$$

We then bridge the two streams by designing a residual fusion mechanism E^{res} that fuses the dynamics into the static reference, and obtain micro-expression features with global dynamics, given by

$$\psi_t = E^{\text{res}}(\psi_1, \Delta\psi_t, t). \quad (5)$$

The final output $\mathcal{M}_t^{\text{init}}$ combines shape, pose, and dynamically-enhanced expression parameters through the FLAME model in Eq. (2).

Motion Encoder: Given an input optical flow sequence $\{\mathcal{O}_t\}_{t=1}^{T-1}$, the motion encoder uses multiple layers of 3D convolution and downsampling to progressively extract spatio-temporal feature maps. The encoder ultimately outputs a sequence of residual expression parameters $\{\Delta\psi_t\}_{t=1}^{T-1}$.

Residual Fusion: We integrate the computed residual expression parameters $\{\Delta\psi_t\}_{t=1}^{T-1}$ into the facial expression parameters ψ_1 of I_1 with global dynamics, and perform residual fusion to operate dynamic integration in a learned latent space. The fusion process begins by projecting the reference expression parameters ψ_1 into a latent representation $z_0 = E^{\text{latent}}(\psi_1)$, where E^{latent} is an encoding network that maps the expression parameters to a lower-dimensional latent space. In this latent space, we use a neural ordinary differential equation (ODE) [40] to model the continuous evolution of expressions, given by

$$\psi_t = D^{\text{latent}}\left(z_0 + \int_0^t E^{\text{ode}}(E^{\text{latent}}(\psi_1), \Delta\psi_\tau, \tau) d\tau\right), \quad (6)$$

where E^{ode} is a neural network, and D^{latent} reconstructs the expression parameters from the latent representation.

B. Dynamic-Guided Mesh Deformation

The dynamic-guided mesh deformation module operates on the initialized meshes $\{\mathcal{M}_t^{\text{init}}\}_{t=1}^T$ and deforms them into the refined meshes $\{\mathcal{M}_t^{\text{final}}\}_{t=1}^T$ through the multi-modal local feature extraction and graph-based mesh deformation, as shown in Figure 3. The refinement process is

$$\mathcal{M}_t^{\text{final}} = \mathcal{G}(\mathcal{M}_t^{\text{init}}, E^{\text{local}}(I_t, \mathcal{O}_t, \mathcal{M}_t^{\text{init}})), \quad (7)$$

where \mathcal{G} represents the graph-based mesh deformation network, and E^{local} denotes the multi-modal feature extraction.

1) *Multi-Modal Local Feature Extraction:* We extract features from multiple cues, yielding more stable and discriminative features of micro-expressions. The motivation is that features from multiple cues capture complementary information, where 3D geometric features preserve spatial consistency, facial priors from landmarks constrain plausible facial deformations, and 2D motion features capture subtle temporal variations.

3D Geometric Features: We construct the adjacency matrix and extract 3D geometric features f_t^{geo} from the initialized mesh $\mathcal{M}_t^{\text{init}}$, given by

$$A_t = \mathcal{A}(\mathcal{M}_t^{\text{init}}), \quad (8)$$

$$f_t^{\text{geo}} = E^{\text{geo}}(\mathcal{V}_t^{\text{init}}, A_t). \quad (9)$$

The adjacency matrix A_t is defined from the graph structure of the initialized meshes $\mathcal{M}_t^{\text{init}}$, which captures the topological

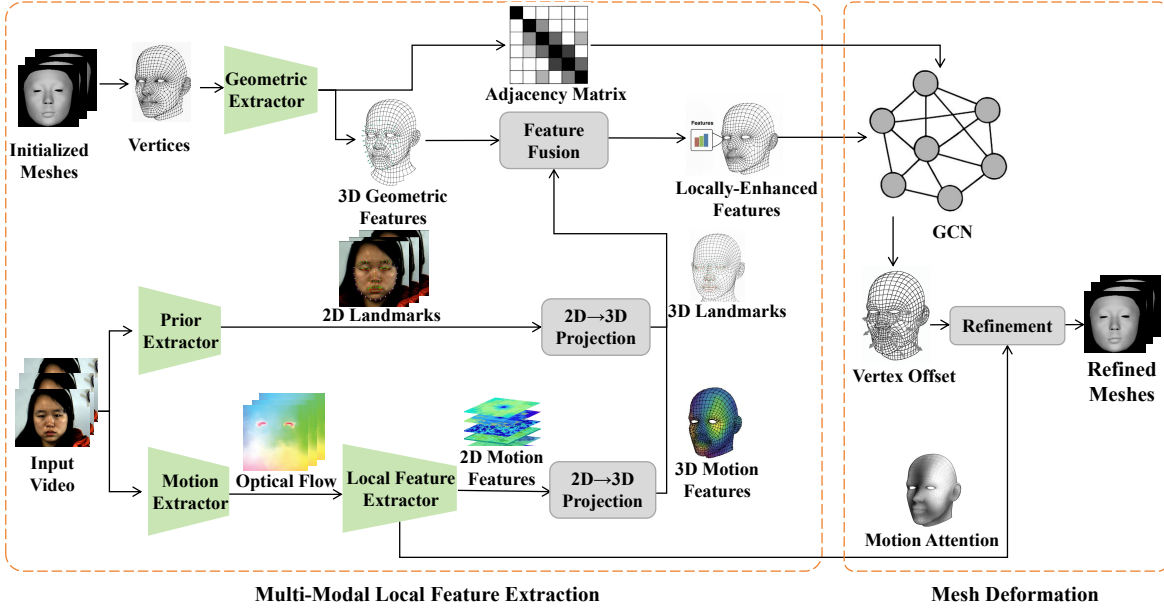


Fig. 3. The *dynamic-guided mesh deformation* module refines the initialized meshes using locally-enriched features to reconstruct subtle dynamic details of micro-expressions.

relationships between vertices. The geometric encoder E^{geo} processes the vertex coordinates through a multi-layer graph convolutional network to extract hierarchical spatial features with the adjacency matrix A_t .

Landmark Features: We use two types of facial landmarks to provide strong facial priors. (1) FAN landmarks l_t^{FAN} with 68 facial keypoints detected using the face alignment network [41], provide comprehensive facial structure coverage. (2) MediaPipe landmarks l_t^{MP} [42] offer enhanced details in critical regions like lips and eyes. The 3D landmark features $f_t^{\text{3D_ldm}}$ are computed by

$$f_t^{\text{3D_ldm}} = \Pi^{-1}(l_t^{\text{FAN}} \oplus l_t^{\text{MP}}, \mathcal{K}), \quad (10)$$

where the projection Π^{-1} uses camera parameters \mathcal{K} to map 2D landmarks to 3D mesh space. The projection ensures anatomical consistency by constraining deformations to physiologically plausible facial configurations while providing strong semantic guidance for local refinement.

Motion-based Features: Motion-based features capture subtle temporal dynamics by processing dense optical flow through a specialized convolutional neural network

$$f_t^{\text{pixel_motion}} = \text{CNN}^{\text{motion}}(\mathcal{O}_t), \quad (11)$$

where $\text{CNN}^{\text{motion}}$ with spatial attention processes the optical flow to extract pixel-level features. To project these pixel-level features to 3D mesh vertices \mathbf{v} effectively, we design an accelerated correspondence strategy that addresses the computational bottleneck of per-vertex projection. Mapping all optical flow pixels to 3D space is computationally inefficient, and we observe that it is not necessary to calculate the 3D motion features of all optical-flow pixels when modeling micro-expressions. To this end, we develop an accelerated region-based pixel-vertex correspondence strategy that significantly reduces computational complexity while maintaining feature discriminability.

Specifically, the facial surface is partitioned into eight semantically meaningful regions \mathcal{R} based on anatomical structure: left eye, right eye, nose, mouth, left cheek, right cheek, forehead, and chin. Each region $r \in \mathcal{R}$ contains a set of vertices \mathcal{V}_r that exhibit similar motion patterns during facial expressions. To efficiently compute motion features, we determine the representative 2D position for each region by calculating its centroid \mathbf{c}_r , given by

$$\mathbf{c}_r = \frac{1}{|\mathcal{V}_r|} \sum_{\mathbf{v} \in \mathcal{V}_r} \Pi(\mathbf{v}, \mathcal{K}), \quad (12)$$

where $\Pi(\mathbf{v}, \mathcal{K})$ denotes projecting all vertices $\mathbf{v} \in \mathcal{V}_r$ from the 3D mesh to the 2D image space. Around each centroid \mathbf{c}_r , we extract a small 5×5 pixel patch \mathcal{P}_r from the motion feature map. This patch \mathcal{P}_r captures the local motion context surrounding the region’s representative position. The region-level motion feature is computed by

$$f_t^{\text{3D_motion}}(\mathbf{v}) = \frac{1}{|\mathcal{P}_r|} \sum_{\mathbf{p} \in \mathcal{P}_r} f_t^{\text{pixel_motion}}(\mathbf{p}), \quad (13)$$

where $r \in \mathcal{R}$ and \mathbf{p} denotes the pixel. Eq. (13) assigns the same region-level motion feature $f_t^{\text{3D_motion}}$ to every vertex \mathbf{v} belonging to the same facial region r .

Feature Fusion: The local features are fused to obtain locally-enhanced features that capture complementary information from different modalities. The fusion begins with feature concatenation followed by a fusion network

$$f_t^{\text{local}} = \text{MLP}^{\text{fusion}}(f_t^{\text{geo}} \oplus f_t^{\text{3D_ldm}} \oplus f_t^{\text{3D_motion}}) \quad (14)$$

The fusion network $\text{MLP}^{\text{fusion}}$ implements a multi-layer perceptron to effectively combine complementary information.

2) *Mesh Deformation:* We use a graph convolutional network (GCN) to process the fused local features and predict vertex-wise displacements. The GCN operates directly on the

mesh graph structure, propagating information through the facial topology defined by the adjacency matrix A_t . The deformation network takes the concatenation of vertex coordinates and local features as input,

$$\mathbf{X}_t^{(0)} = [\mathcal{V}_t^{\text{init}}; J_t^{\text{local}}]. \quad (15)$$

The graph convolution layers then iteratively update vertex features through neighborhood aggregation by

$$\mathbf{X}_t^{(l+1)} = \sigma \left(\tilde{D}^{-\frac{1}{2}} \tilde{A}_t \tilde{D}^{-\frac{1}{2}} \mathbf{X}_t^{(l)} W^{(l)} \right), \quad (16)$$

where $\tilde{A}_t = A_t + I$ is the adjacency matrix with self-connections, \tilde{D} is the degree matrix, $W^{(l)}$ denotes learnable weight matrices, and σ is the ReLU activation function. After L graph convolution layers, the network predicts vertex displacements through an output *MLP*,

$$\Delta \mathcal{V}_t^{\text{base}} = \text{MLP}^{\text{output}}(\mathbf{X}_t^{(L)}). \quad (17)$$

Motion-Attentive Vertex Refinement: To focus on regions exhibiting micro-expression activity, we introduce a motion attention mechanism that adaptively modulates vertex displacements based on optical flow intensity. This mechanism ensures that regions with significant motion receive more refinement while maintaining stability in relatively static areas.

For each vertex \mathbf{v} , the attention weight $\mathbf{W}^{\text{attn}}(\mathbf{v})$ is determined by comparing the flow intensity in its corresponding region against an adaptive threshold. The regional flow intensity $I_t^{\text{flow}}(r)$ is computed as the average magnitude of optical flow within the 5×5 pixel patch \mathcal{P}_r associated with region r , given by

$$I_t^{\text{flow}}(r) = \frac{1}{|\mathcal{P}_r|} \sum_{\mathbf{p} \in \mathcal{P}_r} \|\mathcal{O}_t(\mathbf{p})\|, \quad (18)$$

where $\|\mathcal{O}_t(\mathbf{p})\|$ is the flow magnitude at pixel \mathbf{p} in frame t . Using this regional intensity measure, the attention weight for each vertex \mathbf{v} located in the region r is calculated as

$$\mathbf{W}^{\text{attn}}(\mathbf{v}) = \text{sigmoid} \left(\frac{I_t^{\text{flow}}(r) - \tau^{\text{adaptive}}}{\tau^{\text{adaptive}} + 10^{-4}} \right), \quad (19)$$

where τ^{adaptive} is a dynamic threshold computed per frame using the statistical properties of flow intensity across the entire face,

$$\tau^{\text{adaptive}} = \mu^{\text{flow}} + 0.5\sigma^{\text{flow}}. \quad (20)$$

μ^{flow} and σ^{flow} denote the mean and standard deviation of flow intensity across all facial regions, respectively. This adaptive thresholding ensures that the attention mechanism responds appropriately to varying expression intensities across different video sequences.

The computed attention weights are then applied to modulate the base vertex displacements predicted by the graph convolutional network,

$$\Delta \mathcal{V}_t = \mathbf{W}^{\text{attn}} \odot (\lambda^{\text{attn}} \Delta \mathcal{V}_t^{\text{base}}), \quad (21)$$

where \odot denotes element-wise multiplication and $\lambda^{\text{attn}} = 0.02$ is a scaling factor that controls the overall magnitude of deformation. This scaling ensures subtle adjustments appropriate for capturing the low-intensity dynamics of micro-expressions while preventing excessive mesh distortion.

The final refined mesh is obtained by applying these motion-attentive vertex offsets to the initialized mesh

$$\mathcal{M}_t^{\text{final}} = (\mathcal{V}_t^{\text{init}} + \Delta \mathcal{V}_t, \mathcal{F}_t). \quad (22)$$

C. Optimization Objectives

Our method uses the reconstruction fidelity loss \mathcal{L}^{rec} and geometric regularization loss \mathcal{L}^{geo} for training, given by

$$\mathcal{L}^{\text{total}} = \mathcal{L}^{\text{rec}} + \lambda^{\text{geo}} \mathcal{L}^{\text{geo}}, \quad (23)$$

where λ^{geo} denotes the trade-off parameter.

Reconstruction Fidelity Loss: We use the reconstruction loss between the input frame I_t and the rendered frame \hat{I}_t in Eq. (3) to ensure photometric and perceptual fidelity, including the photometric loss $\mathcal{L}^{\text{photo}}$, VGG perceptual loss \mathcal{L}^{vgg} , landmark loss \mathcal{L}^{lmk} , expression regularization loss \mathcal{L}^{reg} , emotion loss \mathcal{L}^{emo} , expression consistency loss \mathcal{L}^{exp} , and identity consistency loss \mathcal{L}^{id} . For further details, we refer readers to *supplementary materials*.

Geometry Regularization Loss: To maintain mesh quality during refinement, we use the geometry regularization loss λ^{geo} operating directly on the mesh structure and its deformation,

$$\mathcal{L}^{\text{geo}} = \lambda^{\text{lap}} \mathcal{L}^{\text{lap}} + \lambda^{\text{normal}} \mathcal{L}^{\text{normal}} + \lambda^{\text{flow_guide}} \mathcal{L}^{\text{flow_guide}}, \quad (24)$$

where \mathcal{L}^{lap} , $\mathcal{L}^{\text{normal}}$ and $\mathcal{L}^{\text{flow_guide}}$ represent the Laplacian smoothness loss, normal consistency loss and flow-guided local refinement loss, respectively. λ^{lap} , λ^{normal} and $\lambda^{\text{flow_guide}}$ are their trade-off parameters.

The Laplacian smoothness loss encourages smooth surface deformation by minimizing the Laplacian of the mesh displacement, given by

$$\mathcal{L}^{\text{lap}} = \mathbb{E}[\|L\Delta \mathcal{V}_t\|_2^2], \quad (25)$$

where L is the Laplace-Beltrami operator.

The normal consistency loss preserves local surface orientation by maintaining face normal coherence

$$\mathcal{L}^{\text{normal}} = \frac{1}{|\mathcal{F}|} \sum_{f \in \mathcal{F}} (1 - \mathbf{n}_f \mathbf{n}_{f_0}^T), \quad (26)$$

where \mathcal{F} is the set of all triangular faces in the mesh, \mathbf{n}_f is the unit normal of the face f in the refined mesh, and \mathbf{n}_{f_0} is the corresponding face normal in the initialized mesh.

The flow-guided local refinement loss encourages appropriate vertex displacement based on optical flow intensity

$$\mathcal{L}^{\text{flow_guide}} = \mathbb{E}[\|\Delta \mathcal{V}_t\| \mathbf{M}^{\text{low}}] - \lambda^{\text{flow}} \mathbb{E}[\|\Delta \mathcal{V}_t\| \mathbf{W}^{\text{attn}}], \quad (27)$$

where \mathbf{M}^{low} is a binary mask that identifies low-flow regions where $\mathbf{W}^{\text{attn}}(\mathbf{v}) < 0.5$, and $\lambda^{\text{flow}} = 0.1$ is the trade-off parameter.

V. EXPERIMENTS

A. Datasets

We repurpose three high-frame-rate micro-expression recognition datasets, namely CASME [8], CASME II [9], and SAMM [10], for evaluating our method. These datasets have demonstrated the ability to capture subtle and rapid facial

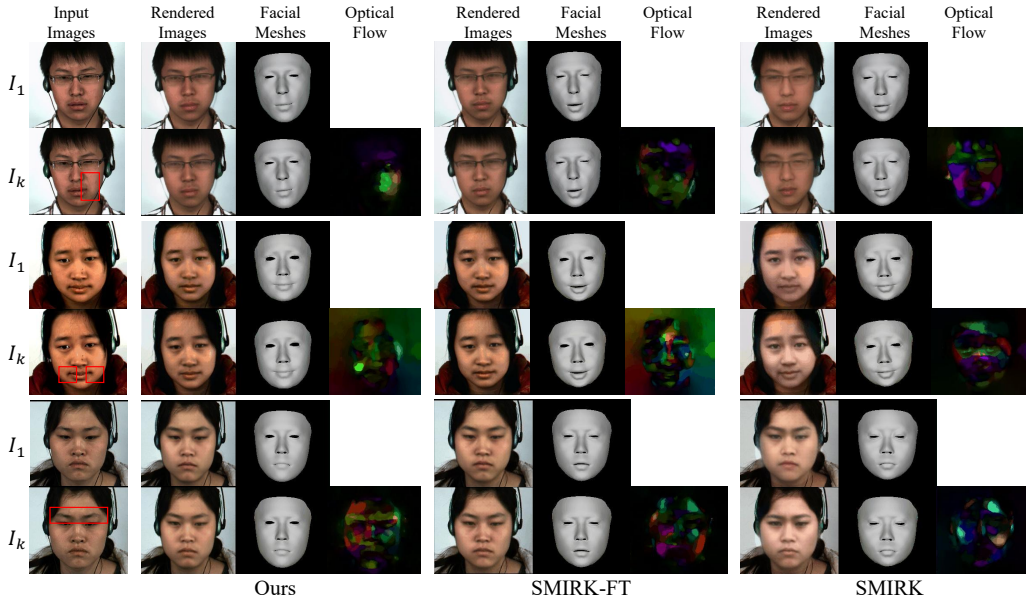


Fig. 4. Visualizations of our method, SMIRK with micro-expression data fine-tuning (SMIRK-FT), and SMIRK without fine-tuning. The red boxes highlight the facial regions where noticeable micro-expression changes occur at I_k .

dynamics that are essential for accurate micro-expression reconstruction. CASME, the pioneering dataset in the CASME series, contains 195 micro-expression videos captured from 26 subjects at 100 fps with natural emotion induction. CASME II contains 255 micro-expression videos captured at 200 fps. SAMM consists of 159 videos recorded at 200 fps under controlled lighting conditions. For each dataset, we randomly select 70% of the videos for training and 30% for testing.

B. Implementation Details

We uniformly sample 8 frames from the onset to offset of each micro-expression clip to capture complete temporal dynamics while reducing redundancy. Frames are aligned and resized to 224×224 . Following SMIRK [5]’s analysis-by-synthesis framework, we first pre-train the static encoder, render and augmented expression cycle path on four macro-expression datasets of FFHQ [43], CelebA [44], LRS3 [45], and MEAD [46]. For micro-expression fine-tuning, we only optimize the dynamic-encoded module and dynamic-guided mesh deformation module using the Adam optimizer [47] with a learning rate $1e - 4$ and batch size 4. Optical flow between frames is computed using TV-L1 [48]. Additional implementation details are provided in the *supplementary material*.

C. Evaluation Metrics

Inspired by the work of SMIRK [5], we use the following metrics to evaluate our method. We evaluate the perceptual quality of rendered micro-expressions in Eq. (3) by measuring the performance of micro-expression recognition using a pre-trained MOL classifier [49], and report accuracy (Acc) and weighted F1-score ($WF1$) for evaluation. We also evaluate the faithfulness of 3D facial reconstruction by comparing the $L1$ Loss and VGG Loss between the rendered images and input

images. We use Fréchet Inception Distance (FID) to measure the perceptual quality between the input images and rendered images.

D. Quantitative Results

We compare our method with state-of-the-art 3D facial expression reconstruction methods, including SMIRK [5], EMOCA [14], and EMICA [50]. To ensure a fair comparison under micro-expression scenarios, we extract the reconstructed meshes from EMOCA and EMICA, and introduce the neural render of the fine-tuned SMIRK (denoted as SMIRK-FT) using micro-expression datasets, to jointly generate the corresponding rendered images in Eq. (3).

As shown in Table I, our method achieves superior performance across all metrics and datasets, demonstrating consistent improvements over existing facial reconstruction methods. In micro-expression recognition, our method achieves 51.77% average accuracy (Acc) with a 5.24% improvement over SMIRK-FT (46.53%), particularly obtaining strong gains in CASME II (+7.50%) and SAMM (+5.88%). The weighted F1 score ($WF1$) similarly improves by 5.16% on average. For reconstruction quality, our method reduces L1 loss by 0.009 (0.048 vs 0.057) and VGG loss by 0.043 (0.660 vs 0.703) on average compared with SMIRK-FT, indicating better detail preservation. In perceptual realism, our method achieves a 9.31 FID improvement (56.78 vs 66.09), with the most significant gain in CASME, compared with the top-performance method SMIRK-FT.

In summary, our method demonstrates clear advantages in capturing subtle micro-expression dynamics while maintaining robust performance across diverse datasets.

E. Qualitative Results

We visualize representative failure cases in Figure ??, which shows the onset and peak frames (input images), rendered

TABLE I
QUANTITATIVE COMPARISON ON MICRO-EXPRESSION DATASETS. BEST RESULTS ARE IN **BOLD**.

Method	CASME II	CASME	SAMM	Avg.
ACC (% ↑)				
EMOCA	40.00	38.93	31.37	36.77
EMICA	42.50	28.81	29.41	33.57
SMIRK	35.00	44.07	45.10	41.39
SMIRK-FT	46.25	42.37	50.98	46.53
Ours	53.75	44.70	56.86	51.77
WF1 (% ↑)				
EMOCA	38.05	28.32	19.74	28.70
EMICA	38.76	21.50	15.38	25.21
SMIRK	32.84	28.65	41.05	34.18
SMIRK-FT	46.35	25.22	49.51	40.36
Ours	53.32	28.65	54.58	45.52
L1 Loss ↓				
EMOCA	0.085	0.196	0.346	0.209
EMICA	0.083	0.197	0.361	0.214
SMIRK	0.085	0.152	0.153	0.130
SMIRK-FT	0.050	0.051	0.069	0.057
Ours	0.041	0.044	0.060	0.048
VGG Loss ↓				
EMOCA	1.578	1.302	1.589	1.490
EMICA	1.501	1.308	1.546	1.452
SMIRK	1.032	1.275	1.260	1.189
SMIRK-FT	0.745	0.567	0.796	0.703
Ours	0.700	0.539	0.742	0.660
FID ↓				
EMOCA	112.37	412.20	448.69	324.42
EMICA	100.04	438.72	469.11	335.96
SMIRK	52.26	349.97	122.13	174.79
SMIRK-FT	33.80	120.28	44.19	66.09
Ours	30.41	100.16	39.76	56.78

facial images and meshes, and the optical flow between input images. In case (a), global motion due to head jitter produces large and noisy optical flow across the entire face, overwhelming the subtle mouth movement and preventing its accurate reconstruction. In case (b), although the optical flow correctly captures eye motion, our FLAME-based mesh lacks detailed 3D modeling of the eye region (e.g., eyelid deformation or eyeball rotation), limiting expressiveness in this area. Cases (c) and (d) illustrate scenarios where the facial motion is extremely subtle. The resulting optical flow magnitude falls below the sensitivity threshold of standard flow estimators, leading to near-zero motion signals and consequently no detectable mesh deformation.

F. Ablation Studies

We conduct comprehensive ablation studies to validate our designs. All experiments are performed on CASME II using the five-class evaluation protocol, and the results are shown in Table II.

Component Analysis: The ablation reveals distinct roles of each component. Removing the dynamic-encoded module (“w/o DEM”) causes the largest accuracy drop (46.25% vs 53.75%) due to its role in temporal dynamics, and removing dynamic-guided mesh deformation (“w/o DGMD”) reduces accuracy by 6.50%. The significant reconstruction quality degradation occurs without pre-training (“w/o Pre-Training”) from the evaluation of L1 Loss, VGG Loss and FID. This demonstrates that pre-training establishes robust facial model-

TABLE II
COMPREHENSIVE ABLATION STUDIES ON MAIN COMPONENTS, MULTI-MODAL FEATURES, AND LOSS FUNCTIONS.

Ablation Type	Acc (%)	WF1 (%)	L1 Loss	VGG Loss	FID
<i>Main Components</i>					
w/o DEM	46.25	46.07	0.042	0.695	30.78
w/o DGMD	47.25	47.28	0.043	0.724	31.70
w/o Pre-Training	50.00	49.85	0.076	0.867	45.95
<i>Multi-modal Features</i>					
w/o Geometry	46.25	45.52	0.042	0.704	31.85
w/o Landmarks	50.00	44.39	0.042	0.702	31.48
w/o Motion	45.00	44.84	0.043	0.699	31.42
<i>Loss Functions</i>					
w/o \mathcal{L}^{geo}	46.25	46.20	0.042	0.701	30.78
w/o \mathcal{L}^{lap}	51.00	50.52	0.043	0.705	30.67
w/o $\mathcal{L}^{\text{normal}}$	48.75	48.36	0.043	0.704	30.66
w/o $\mathcal{L}^{\text{flow_guide}}$	51.25	50.65	0.041	0.700	30.70
Full Model	53.75	53.32	0.041	0.700	30.41

ing foundations, while our specialized modules enable precise micro-expression dynamics extraction.

Feature Analysis: The significant performance drop when removing motion features (“w/o Motion”, 8.75% accuracy decrease) underscores the critical role of dynamics. The removal of geometric and landmark features also reduces performance, confirming that each modality provides unique spatial and facial priors essential for robust reconstruction.

Loss Function Analysis: Geometric regularization losses collectively enhance performance, with \mathcal{L}^{geo} removal causing 7.50% accuracy drop. $\mathcal{L}^{\text{normal}}$ preserves local details, while \mathcal{L}^{lap} and $\mathcal{L}^{\text{flow_guide}}$ ensure smooth deformation and motion-aware refinement, respectively. Therefore, removing any of them reduces recognition accuracy, confirming their complementary roles.

G. Limitation and Discussion

While our method demonstrates good performance in reconstructing micro-expressions, it still presents two main limitations. First, although our region-based acceleration significantly improves efficiency, the per-vertex optimization remains computationally demanding and fails to achieve real-time performance. Since micro-expressions commonly involve only sparse facial regions, exploring sparse-region representations offers a promising direction for further work. Second, optical flow images are often affected by noise, and assigning excessive weight to $\mathcal{L}^{\text{flow_guide}}$ may introduce mesh distortions. Developing more robust strategies to extract micro-expression cues from noisy optical flow constitutes an important avenue for future research. Please refer to the *supplementary materials* for more results and analysis.

VI. CONCLUSION

We have presented a fine-grained method for 3D facial micro-expression reconstruction from monocular videos. The proposed method can address the unique challenges posed by the subtle, transient, and low-intensity nature of micro-expressions. We have devised a dynamic-encoded module that can leverage macro-expression data to alleviate the scarcity

of micro-expression data, along with a dynamic-guided mesh deformation module that can fuse multi-modal local features for detail refinement. Extensive experiments on three datasets of CASME, CASME II, and SAMM can demonstrate the effectiveness of our method.

REFERENCES

- [1] H. Kong, J. Xie, J. Yu, Y. Chen, L. Kong, Y. Zhu, and F. Tang, "Realistic facial expression reconstruction using millimeter wave," *IEEE Trans. Mob. Comput.*, vol. 24, no. 7, pp. 5964–5980, 2025.
- [2] Y. Liu, L. Zhu, L. Lin, Y. Zhu, A. Zhang, and Y. Li, "TEASER: token enhanced spatial modeling for expressions reconstruction," in *Int. Conf. Learn. Represent.*, 2025.
- [3] Y. Hu, B. Chen, J. Lin, Y. Wang, Y. Wang, C. Mehlman, and H. Lipson, "Human-robot facial coexpression," *Sci. Robotics*, vol. 9, no. 88, 2024.
- [4] M. Suguitan, N. DePalma, G. Hoffman, and J. K. Hodgins, "Face2gesture: Translating facial expressions into robot movements through shared latent space neural networks," *ACM Trans. Hum. Robot Interact.*, vol. 13, no. 3, pp. 45:1–45:18, 2024.
- [5] G. Retsinas, P. P. Filntisis, R. Danecek, V. F. Abrevaya, A. Roussos, T. Bolkart, and P. Maragos, "3d facial expressions through analysis-by-neural-synthesis," in *CVPR*, 2024, pp. 2490–2501.
- [6] S. Qian, T. Kirschstein, L. Schoneveld, D. Davoli, S. Giebenhain, and M. Nießner, "Gaussianavatars: Photorealistic head avatars with rigged 3d gaussians," in *CVPR*, 2024, pp. 20299–20309.
- [7] G. Zhao, X. Li, Y. Li, and M. Pietikäinen, "Facial micro-expressions: An overview," *Proc. IEEE*, vol. 111, no. 10, pp. 1215–1235, 2023.
- [8] W.-J. Yan, Q. Wu, Y.-J. Liu, S.-J. Wang, and X. Fu, "Casme database: A dataset of spontaneous micro-expressions collected from neutralized faces," in *IEEE Int. Conf. Worksh. Autom. Face Gesture Recognit.*, 2013, pp. 1–7.
- [9] W.-J. Yan, X. Li, S.-J. Wang, G. Zhao, Y.-J. Liu, Y.-H. Chen, and X. Fu, "Casme ii: an improved spontaneous micro-expression database and the baseline evaluation," *PLoS One*, vol. 9, no. 1, p. e86041, 2014.
- [10] A. K. Davison, C. Lansley, N. Costen, K. Tan, and M. H. Yap, "SAMM: A spontaneous micro-facial movement dataset," *IEEE Trans. Affect. Comput.*, vol. 9, no. 1, pp. 116–129, 2018.
- [11] Z. Ruan, C. Zou, L. Wu, G. Wu, and L. Wang, "Sadmet: Self-aligned dual face regression networks for robust 3d dense face alignment and reconstruction," *IEEE Trans. Image Process.*, vol. 30, pp. 5793–5806, 2021.
- [12] X. Zeng, X. Peng, and Y. Qiao, "Df2net: A dense-fine-finer network for detailed 3d face reconstruction," in *Int. Conf. Comput. Vis.*, 2019, pp. 2315–2324.
- [13] M. Sela, E. Richardson, and R. Kimmel, "Unrestricted facial geometry reconstruction using image-to-image translation," in *Int. Conf. Comput. Vis.*, 2017, pp. 1585–1594.
- [14] R. Danecek, M. J. Black, and T. Bolkart, "EMOCA: emotion driven monocular face capture and animation," in *IEEE Conf. Comput. Vis. Pattern Recog.*, 2022, pp. 20279–20290.
- [15] Y. Feng, H. Feng, M. J. Black, and T. Bolkart, "Learning an animatable detailed 3d face model from in-the-wild images," *ACM Trans. Graph.*, vol. 40, no. 4, pp. 88:1–88:13, 2021.
- [16] S. Wu, C. Rupprecht, and A. Vedaldi, "Unsupervised learning of probably symmetric deformable 3d objects from images in the wild (invited paper)," *IEEE Trans. Pattern Anal. Mach. Intell.*, vol. 45, no. 4, pp. 5268–5281, 2023.
- [17] A. S. Jackson, A. Bulat, V. Argyriou, and G. Tzimiropoulos, "Large pose 3d face reconstruction from a single image via direct volumetric CNN regression," in *Int. Conf. Comput. Vis.*, 2017, pp. 1031–1039.
- [18] A. Chatziagapi, S. Athar, F. Moreno-Noguer, and D. Samaras, "SIDER: single-image neural optimization for facial geometric detail recovery," in *Int. Conf. 3D Vis.*, 2021, pp. 815–824.
- [19] T. Yenamandra, A. Tewari, F. Bernard, H. Seidel, M. Elgharib, D. Cremers, and C. Theobalt, "i3dmm: Deep implicit 3d morphable model of human heads," in *IEEE Conf. Comput. Vis. Pattern Recog.*, 2021, pp. 12803–12813.
- [20] P. Dou, S. K. Shah, and I. A. Kakadiaris, "End-to-end 3d face reconstruction with deep neural networks," in *IEEE Conf. Comput. Vis. Pattern Recog.*, 2017, pp. 1503–1512.
- [21] P. Paysan, R. Knothe, B. Amberg, S. Romdhani, and T. Vetter, "A 3d face model for pose and illumination invariant face recognition," in *IEEE Int. Conf. Adv. Video Signal Based Surveill.*, S. Tubaro and J. Dugelay, Eds., 2009, pp. 296–301.
- [22] C. Li, A. Morel-Forster, T. Vetter, B. Egger, and A. Kortylewski, "Robust model-based face reconstruction through weakly-supervised outlier segmentation," in *IEEE Conf. Comput. Vis. Pattern Recog.*, 2023, pp. 372–381.
- [23] A. Tewari, M. Zollhöfer, H. Kim, P. Garrido, F. Bernard, P. Pérez, and C. Theobalt, "Mofa: Model-based deep convolutional face autoencoder for unsupervised monocular reconstruction," in *Int. Conf. Comput. Vis.*, 2017, pp. 3735–3744.
- [24] P. Selvaraju, V. F. Abrevaya, T. Bolkart, R. Akkerman, T. Ding, F. Amjadi, and I. Zharkov, "OFER: occluded face expression reconstruction," in *IEEE Conf. Comput. Vis. Pattern Recog.*, 2025, pp. 26985–26995.
- [25] T. Büchner, C. Anders, O. Guntinas-Lichius, and J. Denzler, "Electromyography-informed facial expression reconstruction for physiological-based synthesis and analysis," in *IEEE Conf. Comput. Vis. Pattern Recog.*, 2025, pp. 215–227.
- [26] L. Bao, X. Lin, Y. Chen, H. Zhang, S. Wang, X. Zhe, D. Kang, H. Huang, X. Jiang, J. Wang, D. Yu, and Z. Zhang, "High-fidelity 3d digital human head creation from RGB-D selfies," *ACM Trans. Graph.*, vol. 41, no. 1, pp. 3:1–3:21, 2022.
- [27] L. Hu, S. Saito, L. Wei, K. Nagano, J. Seo, J. Fursund, I. Sadeghi, C. Sun, Y. Chen, and H. Li, "Avatar digitization from a single image for real-time rendering," *ACM Trans. Graph.*, vol. 36, no. 6, pp. 195:1–195:14, 2017.
- [28] S. Bharadwaj, Y. Zheng, O. Hilliges, M. J. Black, and V. F. Abrevaya, "FLARE: fast learning of animatable and relightable mesh avatars," *ACM Trans. Graph.*, vol. 42, no. 6, pp. 204:1–204:15, 2023.
- [29] P. Grassal, M. Prinzler, T. Leistner, C. Rother, M. Nießner, and J. Thies, "Neural head avatars from monocular RGB videos," in *IEEE Conf. Comput. Vis. Pattern Recog.*, 2022, pp. 18632–18643.
- [30] C. Wang, D. Kang, Y. Cao, L. Bao, Y. Shan, and S. Zhang, "Neural point-based volumetric avatar: Surface-guided neural points for efficient and photorealistic volumetric head avatar," in *SIGGRAPH Asia*, J. Kim, M. C. Lin, and B. Bickel, Eds., 2023, pp. 50:1–50:12.
- [31] Y. Zheng, V. F. Abrevaya, M. C. Bühler, X. Chen, M. J. Black, and O. Hilliges, "I M avatar: Implicit morphable head avatars from videos," in *IEEE Conf. Comput. Vis. Pattern Recog.*, 2022, pp. 13535–13545.
- [32] C. Chen, M. O'Toole, G. Bharaj, and P. Garrido, "Implicit neural head synthesis via controllable local deformation fields," in *IEEE Conf. Comput. Vis. Pattern Recog.*, 2023, pp. 416–426.
- [33] X. Gao, C. Zhong, J. Xiang, Y. Hong, Y. Guo, and J. Zhang, "Reconstructing personalized semantic facial nerf models from monocular video," *ACM Trans. Graph.*, vol. 41, no. 6, pp. 200:1–200:12, 2022.
- [34] Y. Hong, B. Peng, H. Xiao, L. Liu, and J. Zhang, "Headnerf: A real-time nerf-based parametric head model," in *IEEE Conf. Comput. Vis. Pattern Recog.*, 2022, pp. 20374–20384.
- [35] X. Zhao, L. Wang, J. Sun, H. Zhang, J. Suo, and Y. Liu, "Havatar: High-fidelity head avatar via facial model conditioned neural radiance field," *ACM Trans. Graph.*, vol. 43, no. 1, pp. 6:1–6:16, 2024.
- [36] J. Tang, D. Davoli, T. Kirschstein, L. Schoneveld, and M. Nießner, "GAF: gaussian avatar reconstruction from monocular videos via multi-view diffusion," in *IEEE Conf. Comput. Vis. Pattern Recog.*, 2025, pp. 5546–5558.
- [37] Y. Feng, W. Liu, T. Bolkart, J. Yang, M. Pollefeys, and M. J. Black, "Learning disentangled avatars with hybrid 3d representations," *CoRR*, vol. abs/2309.06441, 2023.
- [38] C. Wang, D. Kang, H. Sun, S. Qian, Z. Wang, L. Bao, and S. Zhang, "Mega: Hybrid mesh-gaussian head avatar for high-fidelity rendering and head editing," in *IEEE Conf. Comput. Vis. Pattern Recog.*, 2025, pp. 26274–26284.
- [39] T. Li, T. Bolkart, M. J. Black, H. Li, and J. Romero, "Learning a model of facial shape and expression from 4d scans," *ACM Trans. Graph.*, vol. 36, no. 6, pp. 194:1–194:17, 2017.
- [40] Y. Rubanova, R. T. Q. Chen, and D. Duvenaud, "Latent odes for irregularly-sampled time series," *CoRR*, vol. abs/1907.03907, 2019.
- [41] A. Bulat and G. Tzimiropoulos, "How far are we from solving the 2d & 3d face alignment problem? (and a dataset of 230,000 3d facial landmarks)," in *Int. Conf. Comput. Vis.*, 2017, pp. 1021–1030.
- [42] Y. Kartynnik, A. Ablavatski, I. Grishchenko, and M. Grundmann, "Real-time facial surface geometry from monocular video on mobile gpus," *CoRR*, vol. abs/1907.06724, 2019.
- [43] T. Karras, S. Laine, and T. Aila, "A style-based generator architecture for generative adversarial networks," in *IEEE Conf. Comput. Vis. Pattern Recog.*, 2019, pp. 4401–4410.
- [44] Z. Liu, P. Luo, X. Wang, and X. Tang, "Deep learning face attributes in the wild," in *Int. Conf. Comput. Vis.*, 2015, pp. 3730–3738.
- [45] T. Afouras, J. S. Chung, and A. Zisserman, "Lrs3-ted: a large-scale dataset for visual speech recognition," *CoRR*, vol. abs/1809.00496, 2018.

- [46] K. Wang, Q. Wu, L. Song, Z. Yang, W. Wu, C. Qian, R. He, Y. Qiao, and C. C. Loy, "Mead: A large-scale audio-visual dataset for emotional talking-face generation," in *Eur. Conf. Comput. Vis.* Springer, 2020, pp. 700–717.
- [47] D. P. Kingma, "Adam: A method for stochastic optimization," *CoRR*, vol. abs/1412.6980, 2014.
- [48] C. Zach, T. Pock, and H. Bischof, "A duality based approach for realtime tv-l 1 optical flow," in *Proc. Joint Pattern recognit. symp.*, 2007, pp. 214–223.
- [49] Z. Shao, Y. Cheng, F. Li, Y. Zhou, X. Lu, Y. Xie, and L. Ma, "MOL: joint estimation of micro-expression, optical flow, and landmark via transformer-graph-style convolution," *IEEE Trans. Pattern Anal. Mach. Intell.*, vol. 47, no. 10, pp. 8756–8768, 2025.
- [50] R. Daněček, K. Chhatre, S. Tripathi, Y. Wen, M. Black, and T. Bolkart, "Emotional speech-driven animation with content-emotion disentanglement," 2023. [Online]. Available: <https://emote.is.tue.mpg.de/index.html>